Colonic epithelial adaptation to EGFR-independent growth induces chromosomal instability and is accelerated by prior injury

Tiane Chen[1,2,*], Maged Zeineldin[1,2,*], Blake Johnson[2,3,4], Yi Dong[2,3], Akshay Narkar[2,3], Taibo Li[4], Jin Zhu[2,3], Rong Li[2,3,5,6], Tatianna C. Larman[1,2**]

[1]Department of Pathology, Division of GI/Liver Pathology, Johns Hopkins University School of Medicine, Baltimore, MD

[2]Center for Cell Dynamics, Johns Hopkins University School of Medicine, Baltimore, MD

[3]Department of Cell Biology, Johns Hopkins University School of Medicine, Baltimore, MD

[4]Medical Scientist Training Program, Johns Hopkins University School of Medicine, Baltimore, MD

[5]Department of Chemical and Biomolecular Engineering, Johns Hopkins University

[6]Mechanobiology Institute and Department of Biological Sciences, National University of Singapore

*These authors contributed equally to this work

**Correspondence: Tatianna C. Larman; 855 N Wolfe St, Rangos 453, Baltimore 21205; O (410-614-5143); F(410-955-0394); tlarman1@jhmi.edu; @tashalarman

RUNNING TITLE

Adaptation to EGFR deficiency induces chromosomal instability in normal colonic epithelium

FUNDING

AACR Never Too Young Early Onset Colorectal Cancer Coalition (T.C.L.), Johns Hopkins Conte Digestive Diseases Basic and Translational Research Core Center Pilot Project Funding (T.C.L.), GI Cancer SPORE Pilot Project Funding (T.C.L.), Sanfilippo Resident Research Award (T.C.L.), Catherine and Constantinos J. Limas Research Award (T.C.L.), NIH Medical Scientist Training Program Award T32 GM007309 (B.J., T.L.).

CONFLICT OF INTEREST

The authors declare no competing interests.

AUTHOR CONTRIBUTIONS

Conceptualization, T.C.L., R.L.; Supervision, T.C.L. and R.L.; Investigation, T.C., M.Z., T.C.L., R.L.; Resources, A.N., B.J. T.L., and Y.D.; Data Curation, T.L.; Visualization, T.C., M.Z., T.L., B.J., T.C.L.; Validation, J.Z., M.Z.; Writing—Original Draft, T.C., T.C.L.; Writing—Review and Editing, T.C., M.Z., T.C.L., R.L.; Funding acquisition, T.C.L., R.L.

ABSTRACT

Although much is known about the gene mutations required to drive colorectal cancer (CRC) initiation, the tissue-specific selective microenvironments in which neoplasia arises remains less characterized. Here, we determined whether modulation of intestinal stem cell niche morphogens alone can exert a neoplasia-relevant selective pressure on normal colonic epithelium. Using adult stem cell-derived murine colonic epithelial organoids (colonoids), we employed a strategy of sustained withdrawal of EGF and EGFR inhibition to select for and expand survivors. EGFR-signaling-independent (iEGFR) colonoids emerged over rounds of selection and expansion. Colonoids derived from a mouse model of chronic mucosal injury showed an enhanced ability to adapt to EGFR inhibition. Whole-exome and transcriptomic analyses of iEGFR colonoids demonstrated acquisition of deleterious mutations and altered expression of genes implicated in EGF signaling, pyroptosis, and CRC. iEGFR colonoids acquired dysplasia-associated cytomorphologic changes, an increased proliferative rate, and the ability to survive independently of other required niche factors. These changes were accompanied by emergence of aneuploidy and chromosomal instability; further, the observed mitotic segregation errors were significantly associated with loss of interkinetic nuclear migration, a fundamental and dynamic process underlying intestinal epithelial homeostasis. This study provides key evidence that chromosomal instability and other phenotypes associated with neoplasia can be induced *ex vivo* via adaptation to EGF withdrawal in normal and stably euploid colonic epithelium, without introducing cancer-associated driver mutations. In addition, prior mucosal injury accelerates this evolutionary process.

Keywords

Intestinal organoids; transformation; chromosomal instability; colorectal cancer; colitis

Key definitions:

Colonoids: adult stem cell-derived colonic epithelial organoids

iEGFR: *in vitro* selective conditions devoid of EGF (epidermal growth factor) and including an EGFR (EGF receptor) inhibitor [1]

iEGFR colonoids: colonoids tolerant to iEGFR culture conditions with growth and survival similar to unselected passage-matched controls

INM: Interkinetic nuclear migration

INTRODUCTION

While much is known about the molecular features of CRC and their adenomatous precursors, it remains a mystery how neoplasia arises from normal epithelium[2,3]. The colonic epithelial crypt is a test-tube shaped unit comprised of Lgr5^{+} stem cells at its base, with its differentiation axis determined by epithelial and stromal microenvironment-derived gradients of niche growth factors[4–6]. How perturbations to normal niche growth factor homeostasis may act to promote or constrain initiation of epithelial neoplasia remain largely unexplored.

Advances in intestinal organoid culture have provided profound insights into the niche signaling pathways required for maintenance of epithelial homeostasis, including the EGFR/MAPK, Wnt, Notch, PI3K, and TGF-β pathways[7]. Intriguingly, these same pathways are recurrently altered in colorectal cancer (CRC), which is in turn characterized by epithelial architectural complexity, niche remodeling, and progressive loss of dependence on key niche factors[2,3,8,9]. Organoid cultures derived from adenomatous precursors and CRC demonstrate heterogeneous patterns of niche factor-independent growth reflective of underlying molecular changes[3,8]. For example, unlike normal epithelial cells, the vast majority of adenoma and CRC cells grow independently of Wnt and R-spondin *ex vivo*, underscoring the fact that *APC* mutation is a common first hit[3]. Further, multiple groups have leveraged the intestinal organoid model to reconstitute the adenoma-carcinoma sequence *in vitro*, harnessing selective strategies to identify successfully edited clones; for example, *KRAS* or *PIK3CA* mutant organoids survive in EGF-deficient conditions[10–12].

The positioning of cells in the intestinal crypt dictates cell fate[13]. Interkinetic nuclear migration (INM) has recently been shown to contribute to the dynamics of cell positioning in the intestinal crypt[14]. INM is a homeostatic mitotic mechanism in intestinal epithelium by which basally located nuclei migrate to the apical aspect of the cell for mitosis, then return to a basal cytoplasmic location after separation of mitotic sisters[14]. Interestingly, loss of INM in *Apc* mutant murine intestinal organoids resulted in placement of mitotic sisters directly adjacent to one another, rather than the physically separated mitotic sisters seen in wild-type mitoses with intact INM[14]. Thus, in addition to altered niche growth factor homeostasis, biophysical factors related to mitotic dynamics, cell geometry, and/or microenvironmental stiffness may also directly contribute to clonal expansion of crypt cell populations to promote neoplasia. In the human colon, cycles of mucosal injury and repair (for example, in inflammatory bowel disease, or IBD) can transiently or permanently alter the biophysical properties, cell populations, and growth factors present in the mucosal microenvironment[15]. Although the mechanisms

are not fully elucidated, such chronic inflammatory insults lead to increased risk for CRC and other epithelial cancers[16,17].

Here we tested the hypothesis that disturbances to the mucosal microenvironment alone have capacity to lead to epithelial-autonomous molecular changes promoting cancer. As the feasibility of short-term EGF withdrawal in organoid culture has been demonstrated[1], EGF is a critical intestinal stem cell niche factor[7,18–20], and EGF signaling is indispensable for normal intestinal stem cell survival and propagation *in vitro*[3,7], we focused our selection experiments on the evolution of EGFR-signaling-independent growth. Indeed, our data show that long-term withdrawal of EGFR signaling alone results in a molecularly distinct and sustained adaptive epithelial phenotype.

METHODS

Mouse Strains Used to Derive Colonoid Lines

Primary colonoid cultures used in this study were derived from C57BL/6J mice (directly received from Jackson Laboratory). All animal experiments were implemented in accordance with an animal protocol approved by the Johns Hopkins University Animal Care and Use Committee (Protocol MO18M85) and ARRIVE (Animal Research: Reporting of *In Vivo* Experiments) guidelines. All the mice were housed in a specific pathogen-free (Helicobacter negative) environment. The DSS chronic colitis mouse model was established as has been described previously with minor modifications[21–23]. In short, male mice 6-8 weeks old were treated with 4 rounds of DSS challenge, each consisting of 5 days of DSS in drinking water (2%, 40 kDa) followed by 7 days of recovery (Alfa Aesar #J63606).

Colonoid Culture

We derived colonoids from normal wildtype C57BL/6 mice (referred to hereafter as control colonoids). Colonoids were derived from the distal 2.5 cm of grossly normal appearing C57BL/6J mouse colons (females 26 weeks old for control and *Apc*^{mut} colonoid lines). Absence of deleterious coding mutations was confirmed by whole-exome sequencing (data not shown). Notably, mouse colons lack Paneth cells, a potential source of EGF[24]. Colonic crypts were isolated and cultured as described previously[7,10]. Colonoids were plated within Matrigel (Corning #356231). Basic culture medium was composed of advanced Dulbecco's modified Eagle's medium/F12 (Gibco™) supplemented with penicillin/streptomycin, 10 mM HEPES (Gibco™ #15630080), GlutaMAX supplement (Gibco™ #35050061), B27™ Supplement (Gibco™ #17504044) and 1 mM N-acetylcysteine (Sigma-Aldrich #A9165). WENR medium was made of basic culture medium (20% final volume), Wnt3a-conditioned media (50% final volume with 5% final FBS concentration, L Wnt-3A ATCC® CRL-2647), and R-Spondin1-conditioned media (20% final volume), Noggin-conditioned media (10% final volume) and EGF (50 ng/mL). WNR medium had EGF omitted. Colonoids were maintained and propagated in culture as described previously[7].

Colonoid transfection and genome editing

The colonoid lipofection and CRISPR/Cas9 genome editing protocol was followed as described previously[25,26]. The sgRNA sequence targeting *Apc* can be found in Supplementary Figure 3A. As described previously, single colonoid survivors in Wnt/R-spondin-deficient media were manually picked and clonally expanded under the same selective conditions. The presence of biallelic truncating mutations at the expected site was confirmed by Topo cloning and whole-exome sequencing (Supplementary Figure 3B). Off-target coding mutations were not detected (data not shown).

158 **Derivation of iEGFR-tolerant organoids**

159 Three days after plating in Matrigel, passage-matched colonoids were switched from WENR to iEGFR
160 media (WNR with 5 μM Gefitinib; Santa Cruz #sc-202166). This concentration of gefitinib was required
161 to kill >90% of normal colonoids at 7 days (data not shown) and was previously used to achieve iEGFR
162 intestinal organoid culture conditions[1]. Fresh media with the drug was added every other day. Survivors
163 were collected after 7 days and allowed to expand in WNR media before re-challenging in iEGFR
164 selection for another 7 days. These cycles of selection and expansion were repeated until the survival
165 rate plateaued (iEGFR-tolerant colonoids). All control colonoids were treated with similar concentration
166 and volume of the compound dissolvent, dimethyl sulfoxide (DMSO, Corning® #25-950-CQC). Control
167 colonoids were maintained in WENR media, and iEGFR-tolerant colonoids were maintained in WNR
168 media long-term. Brightfield images of each cycle were captured on day 0 and day 7 using a Zeiss
169 Microscope (Carl Zeiss Axiovert 40 C) with a 4x objective and the iDu Optics LabCam Microscope
170 Adapter for iPhone8+ (iDu Optics). Quantification of survival rate was carried out manually. At the
171 beginning of each cycle, the total number of colonoids in both control and treatment groups were
172 counted under the microscope with a cell counter based on visual inspection (see images in
173 Supplementary Figure 3D). At the end of each selection cycle (7 days), the total number of live
174 colonoids in each well of both groups was counted. Survival rate was calculated as the total number of
175 live colonoids post-treatment at day 7 to total number of colonoids pre-treatment at day 0 in each well.
176 The relative survival rate was generated by comparing survival to untreated controls.

177

178 **Histology**

179 Whole colonoids were collected by gently dissolving Matrigel in ice-cold PBS (pH 7.4), and
180 subsequently fixed for 30 min at room temperature in 4% paraformaldehyde (16% PFA, Pierce™
181 #28906). Colonoids were then washed with PBS (pH 7.4) at room temperature. Colonoids were
182 pelleted and transferred to the top of 2% solidified agarose gel in a 0.5 mL microfuge tube (Sigma-
183 Aldrich #A9539). After aspiration of PBS, another 100uL of warm agarose gel was added to the
184 colonoids. After gel solidification, the entire microcentrifuge tube was placed into a 15 mL conical
185 containing 10 mL buffered 10% formalin (Sigma-Aldrich #HT501128) overnight. The bottom of the
186 microcentrifuge tube was carefully removed with a razor blade and the colonoid block was transferred
187 into a tissue cassette and submitted for paraffin embedding. 4 μm thick sections were stained with
188 hematoxylin and eosin (performed by the Johns Hopkins Oncology Tissue Services Core).
189 Photomicrographs of colonoids and deidentified human tissue samples (in accordance with the Johns
190 Hopkins University School of Medicine Institutional Review Board, IRB00273344) were taken using an
191 Olympus BX46 upright microscope and Teledyne Lumenera Infinity Analyze software.

192 **Metaphase spreads**

193 Colonoids were treated with 100 μM colcemid (Gibco™ #15212012) for 4 hours and dissociated with
194 800 μL of TrypLE (Gibco™ #12604013) and Accutase (Invitrogen™ #00-4555-56) (1:1 ratio) for 10–15
195 min at 37 °C. After washout of TrypLE and accutase with advanced DMEM/F12 medium (Gibco™
196 #12634010) containing HEPES buffer (Gibco™ #15630080, 1 mM), penicillin/streptomycin (Gibco™
197 #15140122, 1%), GlutaMax (Gibco™ #35050061, 0.2 mM), cells were treated with pre-warmed KCl
198 (0.56%) for 15 min at room temperature. Subsequently, 120 μl of fixative solution (methanol:acetic acid;
199 3:1) were added before centrifuging. After centrifugation, 10 ml fixative solution were slowly added
200 before incubation at 4°C overnight. Fixed cells were dropped onto a glass microscope slide using a 20-
201 μl pipette, air dried, and heat-dried (65°C) for 60 min. Slides were then incubated for 1 hour at 37 °C in
202 propidium iodide (PI)/RNase staining buffer and rinsed with ddH_2O. Slides were mounted with
203 Vectashield containing DAPI (Vector Labs #H-1000) and analyzed on a Nikon laser microscope (×60
204 Super-Plan APO oil 1.4 NA objective). Control colonoids were assayed at passages 8 and 15; iEGFR
205 colonoids were assayed at passage 40 (low, L) and passage 66 (high, H); *Apc*^{mut} colonoids were
206 assayed at passages 28 and 30; DSS control colonoids were assayed at passages 5, 15, and 35; and
207 DSS iEGFR colonoids were assayed at passages 15 and 35. Results were similar across passage
208 numbers and combined per group, with the exception of iEGFR colonoids (as noted in Figure 4A).
209 Chromosomes from each spread were manually counted in a blinded manner using Fiji/ImageJ.
210

211 **3D immunostaining and clearing of organoids**

212 Whole colonoids were collected by gently dissolving Matrigel in ice-cold PBS and fixed for 30 min at
213 room temperature in 4% paraformaldehyde (PFA, Sigma). Colonoids were then transferred to organoid
214 washing buffer (PBS containing 0.1% Triton X-100 and 0.2% BSA), then distributed into a 24-well plate.
215 For immunofluorescent staining, colonoids were permeabilized and blocked in PBS containing 0.5%
216 Triton X-100 and 1% BSA (Sigma) for 1 hour at room temperature, then incubated in blocking buffer
217 containing primary antibody overnight at 4°C. Primary antibodies used were Chromogranin A (Santa
218 Cruz #Sc-1488) and phospho-histone H2A.X (Ser139; Cell Signaling Tech #2577). Colonoids were
219 incubated with corresponding secondary antibody Alexa 488 anti-mouse IgG (Invitrogen™ #A11029), in
220 blocking buffer for overnight at 4°C, with 1ug/ul DAPI added for the final 15 minutes of incubation.
221 Colonoids were washed 4-5 times (2 hours each), then cleared in fructose-glycerol clearing buffer (60%
222 (vol/vol) glycerol and 2.5 M fructose) for 15 mins before imaging on a Zeiss LSM 780 confocal
223 microscope[27]. Image analysis was performed using Zen and Fiji/ImageJ software.
224
225

226 **EdU incorporation assay**

227 Colonoids were plated in an 8-well Chamber Coverglass (Nunc™ Lab-Tek™, Cat#155411). 4-5 days
228 after plating, EdU (10 μM) was added to fresh medium for 6 hours. Colonoids were then fixed with
229 warm 4% PFA for 10 mins at 37ºC, then rinsed once with room temperature PBS. Blocking and
230 permeabilization buffer (PBS containing 1% BSA and 0.5 % Triton X-100) was added for 2 hours at
231 room temperature. EdU detection reagents were then added for 2 hours at room temperature in the
232 dark (Click-iT™ Assay Kit, Sigma-Aldrich #C10337). Nutlin was used as a positive control (Selleckchem
233 #S7101). Images were captured with the Zeiss LSM780 confocal microscope (40x/1.4 NA objective).
234 Image analysis was performed using Zen, Fiji/ImageJ and Imaris software.

235

236 **Four-dimensional colonoid imaging and image analysis**

237 **Lentivirus production:** The plasmids used were pMD2.G (Addgene plasmid RRID# 12259), psPAX2
238 (Addgene plasmid RRID#12260), and pLV-H2B-Neon-ires-Puro (kindly gifted by the Hugo J.G. Snippert
239 and Geert J.P.L. Kops laboratories of the University Medical Center Utrecht). To make lentivirus
240 particles, HEK 293FT cells were co-transfected with the lentiviral transfer plasmid, packaging plasmid,
241 and envelope plasmid. Media containing lentivirus was collected 24 and 48 hours after transfection.
242 Lentivirus was concentrated using a centrifugal filter (Amicon Ultra-15, 100,000 NMWL). The lentiviral
243 titer was determined by qPCR (abm qPCR Lentivirus Titration Kit, cat. # LV900). Viral titers used in this
244 study ranged from $1x10^8$-$1x10^9$ IU/ml.

245

246 **Lentiviral infection of colonoids:** To visualize mitoses, colonoids were infected with lentivirus
247 encoding mNeon-tagged histone 2B and a puromycin resistance cassette described above. The
248 protocol was performed as described previously with minor modifications[28]. Briefly, colonoids ~100 μm
249 in diameter were transferred to a 15 ml tube and pelleted (1000 rpm for 5 minutes) before single cell
250 dissociation (600-800μL TrypLE, 37˚C). Pelleted single cells were resuspended in 1 ml of prewarmed
251 infection medium, consisting of 500μL concentrated virus, 500 μl WENR (control colonoids), WNR
252 (iEGFR colonoids), or Wnt/R-spondin deficient media (*Apc*^{mut} colonoids), 8 μg/ml Polybrene (Sigma-
253 Aldrich #TR-1003), and 10 μM Rock inhibitor Y-27632 (Sigma-Aldrich #Y0503), then centrifuged at 100
254 rpm for 1h at room temperature. Colonoids were then transferred to the cell incubator (37°C, 5% CO2)
255 for 5–6 hours and gently remixed every hour prior to replating with fresh media as indicated.
256 Approximately 2-3 days after infection, the expression of transduced fluorescence protein was
257 observed and puromycin selection (1 μg/mL) was initiated. Puromycin was increased to 5ug/mL once
258 colonoid size reached more than 100 μm.

259

260 **Four-dimensional colonoid imaging:** After two passages of puromycin selection, colonoids were
261 dissociated using TrypLE and replated in an 8-well glass-bottom chamber slide (Nunc™ Lab-Tek™,
262 Cat#155411). Three to four days later, the chamber was mounted on a confocal laser-scanning
263 microscope (LSM 780), which was continuously held at 37 ºC with 5.0% CO_2. H2B-Neon-positive
264 organoids were imaged in xyzt mode for 16–18h at 37°C at 3 min intervals using a 40x water-
265 immersion objective (NA 1.1). Eight to ten H2B-mNeon-expressing colonoids were imaged
266 simultaneously using minimal amounts of 488 nm laser excitation. In total, 14-16 z-sections at 2-µm
267 intervals were imaged per colonoid.
268
269 **Imaging analysis:** To analyze mitoses, raw image Z-stacks were converted to depth color-coded
270 maximum projections with using a custom macro modified from the ImageJ/Fiji software plugin
271 "Temporal-Color Code"[29]. The macro attributes a color code to each z-layer, facilitating visual
272 discrimination of cells overlapping in XY as described previously[10]. Data sets were converted into
273 manageable and maximally informative videos, combining z-projection, depth color-coding and merging
274 with transmitted light images (Supplementary Videos 1–6). Mitoses were blinded and scored, judged
275 and counted manually by both T.C. and T.C.L. For analysis of interkinetic nuclear migration, Fiji/ImageJ
276 was used to measure the pixel distance the basal aspect of a nucleus moved prior to mitotic entry and
277 nuclear envelope breakdown. Any distance moved was categorized as intact interkinetic nuclear
278 migration. No measurable movement was categorized as loss of interkinetic nuclear migration.
279
280 **Quantitative RT-PCR based mouse karyotyping**
281 SYBR Green qPCR assays were designed and validated for every mouse chromosome based on
282 GRCm38/mm10 genome assembly (primer sequences listed in Table S1). qPCR reactions were set up
283 in triplicate in a 384-well plate and run on the CFX384 Touch Real-Time PCR Detection System (Bio-
284 Rad). Each reaction contained 5µL of PerfeCTa SYBR Green FastMix (Quantabio, catalog number
285 95073-05K), 2.5µL of forward and reverse primer mix at 2µM, 0.5µL of purified genomic DNA at 1ng/µL
286 and 2µL of nuclease-free water. A standard cycling protocol was followed as provided with the SYBR
287 Green reagent. Ct values were acquired with CFX Manager Software (Bio-Rad) and the relative
288 chromosome copy numbers were calculated using a modified ΔΔCt method as described previously[30].
289
290 **RNA sequencing**
291 Total RNA was isolated from pelleted colonoids in using Trizol (Invitrogen™ #15596026) according to
292 the manufacturer's instructions and purified using the Purelink RNA Mini Kit (Invitrogen™ #12183018A).
293 RNA-sequencing data were generated by Novogene. cDNA libraries were sequenced on an Illumina

294 NextSeq500 using 75-bp paired-end sequencing. Clean reads were mapped to UCSC GRCm38
295 reference genome using STAR v2.5 software[31] and raw counts were assigned to Ensembl genes using
296 featureCounts (subread v2.0.0 aligner command line tool)[32]. Differential gene analysis was performed
297 using DESeq2 v1.28.1 following regularized logarithm transformation of raw count data[33]. Gene set
298 enrichment analysis (GSEA) was performed using the gost function of the R package gprofiler2
299 v0.1.9[34]. Genes were considered differentially expressed and included in the GSEA if they had a *p*-
300 value <3.3e-7 (Bonferroni adjusted) and an absolute $\log_2$-transformed fold change >2. Statistical
301 analysis and plotting were performed using R software (version 3.4.0). Statistical significance was
302 assessed at α=0.05. The significance level for differential gene analysis was adjusted using the
303 Bonferroni approach while also accounting for multiple comparisons across experimental conditions
304 (threshold *p*=3.3e-7). All data are presented as mean ± SEM. Analysis of two samples was performed
305 with unpaired two-tailed student t-test for equal variance, or t-test with Welch's correction for
306 heterogeneity of variance.
307
308 **Whole Exome sequencing**
309 DNA was extracted from pelleted colonoids using the Purelink Genomic DNA Kit (Invitrogen™ #K1820-
310 01) according to the manufacturer's instructions. Whole exome sequencing data were generated by
311 BGI. In short, fragmented gDNA was subjected to adapter ligation, amplification, and exome array
312 hybridization. Captured products were circularized and DNA nanoballs were produced using rolling
313 circle amplification prior to loading onto the BGISEQ sequencing platform. Mean sequencing depth on
314 target regions was 117.58x, and 98.69% of targeted bases had at least 10x coverage. Paired-end
315 reads were mapped to UCSC GRCm38 and aligned using Burrows-Wheeler Aligner (BWA) software.
316 The Genome Analysis Toolkit (GATK) was used for variant calling and the SnpEff tool was used for
317 variant annotation. Variants of interest were filtered based on >10x depth of coverage, predicted high
318 functional impact (MutDB), and visual inspection using Integrative Genomics Viewer (IGV).
319
320 **Quantitative RT-PCR**
321 cDNA was isolated using SuperScript™ III Reverse Transcriptase (Invitrogen # 108080) following the
322 manufacturer's protocol. A dilution series of cDNA was used to validate the primer pairs, and both
323 melting curve analysis and agarose gel electrophoresis were performed to check for specificity of
324 primers (data not shown). Quantitative PCR was performed using the SYBR green Select Master Mix
325 (Thermo Fisher #4472908) following the manufacturer's protocol. Each sample was done in triplicate in
326 a total reaction volume of 10-µl containing 0.5-µl of 1:8 diluted cDNA (validated dilution with dynamic
327 range of amplification) and 5nM primer mix using the CFX384 QPCR machine (Biorad). The list of

328 primers used are listed in Supplementary Table 3. Delta (Cq) was calculated by subtracting the mean
329 Cq for every tested gene to those of the internal control genes (*Hprt* and *ActB*). Log fold change was
330 calculated by subtracting Delta(Cq) of iEGFR samples from those of controls.

331

332

333

334

335

336

337

338

339

340

341

342

343

344

345

346

347

348

349

350

351 **RESULTS**

352 **Normal murine colonoids can achieve sustained EGFR-independent growth in long-term culture**
353 We tested our hypothesis that changes in the availability of niche factors can select for a cancer
354 phenotype in normal wild-type colonic epithelium using colon-derived organoids (colonoids). To select
355 for EGFR-independent growth *in vitro*, we cultured normal colonoids from wild-type mice ("control"
356 colonoids) in EGF-depleted (WNR) medium with the EGFR-specific inhibitor Gefitinib; we refer to these
357 culture conditions as iEGFR. The EGFR inhibitor was used to address the possibility of
358 autocrine/paracrine production of EGF by the cultured colonoids or the presence of exogenous EGF in
359 the 5% final concentration of fetal bovine serum in EGF-depleted medium. Over 7 days, iEGFR
360 selection resulted in the death of most colonoids. Rare survivor colonoids appeared smaller and lacked
361 budding compared to control colonoids, suggesting that they were mostly quiescent[1]. These survivors
362 were recovered and expanded in WNR media, but not in the presence of Gefitinib. We continued to re-
363 challenge the expanded survivors with additional 7-day cycles of iEGFR selection. Increasing numbers
364 of survivors were recovered with each re-challenge cycle (Figure 1A), and approximately half of
365 colonoids survived after 3 cycles of selection. A total of 5 cycles were required to achieve complete
366 EGFR-independent growth (iEGFR colonoids), with survival rate similar to unchallenged colonoids in
367 EGF-replete media (Figure 1A). Notably, we also observed a transient enrichment of cells with
368 enteroendocrine differentiation during iEGFR selection as reported previously (Supplementary Figures
369 1A-B)[1]. We continuously propagated iEGFR colonoids for 8 months in WNR medium.
370
371 To test whether iEGFR tolerance was reversible after relaxing selective conditions, we returned iEGFR
372 colonoids to EGF-replete medium (WENR) for 3 weeks. Surprisingly, approximately 70% of iEGFR
373 colonoids died each week in the presence of EGF compared to those maintained in the WNR medium.
374 Moreover, removal of EGF from the culture reverted to the growth of iEGFR colonoid baseline of near-
375 100% survival (Supplemental Figure 1C). Taken together, our data demonstrate the feasibility of
376 evolving and propagating growth factor-independent colonic epithelium. They also show that the
377 resulting phenotype is a stable trait that does not require persistent selection once acquired with an
378 acquired and related vulnerability.
379
380 **Prior epithelial injury facilitates adaptation to iEGFR selection**
381 We tested whether chronic injury and repair can influence adaptability to EGF deprivation using
382 colonoids generated from a mouse model of chronic chemical colitis (DSS, dextran sodium sulfate). As
383 previously described[35], these mice showed cardinal signs of colitis as manifested by a significant

384 reduction in the ratio between body weight to colon length (Supplementary Figure 2A) and histologic
385 features (Supplementary Figure 2B). Colonoids derived from DSS-treated mice more readily adapted to
386 iEGFR selection compared to controls, with approximately 60% of colonoids surviving the first 7 day
387 cycle of selection compared to approximately 10% of control colonoids (Figure 1A). In addition, DSS
388 colonoids reached a survival plateau after only 2 cycles of iEGFR selection (Figure 1B), compared to 5
389 cycles for control colonoids. These data indicate that prior exposure to cycles of mucosal injury *in vivo*
390 primed colonic epithelium for adaptation to iEGFR selection.
391
392 **iEGFR colonoids acquire tolerance to deprivation of other niche factors**
393 To test whether iEGFR colonoids more readily acquire additional niche factor independence, we
394 challenged them in medium lacking Wnt/R-spondin, as well as in a base medium that additionally lacks
395 Noggin. The majority of iEGFR colonoid lines survived this selective challenge after a week (Figure 1B,
396 Supplementary Figure 3D). On the other hand, the majority of control colonoids did not survive either
397 condition. These data demonstrate that iEGFR colonoids acquired the capacity to tolerate additional
398 niche-relevant selective pressures.
399
400 ***Apc* mutant colonoids are more vulnerable to EGF-deficient conditions**
401 Mathematical modeling of CRC carcinogenesis suggests that *APC* mutations may accelerate the
402 acquisition of subsequent molecular alterations[36]. If iEGFR adaptation relies upon *de novo* oncogenic
403 mutation, *Apc* loss should confer an adaptive advantage. To test this hypothesis, we introduced biallelic
404 truncating mutations in *Apc* via CRISPR/Cas9 genome editing to a control mouse colonoid line
405 (Supplementary Figure 3A-B, confirmed by whole exome sequencing). As previously described, *Apc*
406 mutant (Apc^{mut}) colonoids grew independently of Wnt/R-spondin-containing medium and adopted
407 spheroid morphology (Figure 1B and Supplemental Figure 3C)[25]. Surprisingly, when Apc^{mut} colonoids
408 were subjected to cycles of iEGFR selection, unlike wild type colonoids, Apc^{mut} colonoids could not
409 adapt to EGF deprivation (Figure 1A). These data suggest that *Apc* loss greatly enhances the
410 sensitivity of colonoids to EGFR deprivation.
411
412 **iEGFR colonoids acquire somatic mutations and transcriptional reprogramming**
413 To determine whether mutations associated with EGF-independent growth may have contributed to the
414 iEGFR phenotype, we performed whole exome sequencing on iEGFR colonoids and controls. First, we
415 looked at mutations in the EGFR signaling pathway that are frequently observed in CRC. No mutations
416 or indels in *Egfr, Kras,* or *Pik3ca* were detected in iEGFR colonoids. However, we detected a coding
417 mutation with predicted high functional impact in *Wnk2,* a negative regulator of EGF-induced activation

418 of ERK/MAPK signaling[37]. iEGFR colonoids also showed predicted deleterious mutations in *Btk,* known
419 to have a role in negatively regulating Wnt-β-catenin signaling[38], *Treml2, and Olfr1255* (Table 1). Mining
420 publicly available data reveals that these genes are altered at very low frequency (<1%) in human
421 CRC, with the exception of *Olfr1255* (Table 1). DSS iEGFR colonoids were enriched for a mutation in
422 *Ninein* (Table 1), a gene involved in centrosomal biology and mitotic fidelity[39]. DSS colonoids did not
423 accumulate coding mutations compared to control colonoids.
424
425 We also performed RNA-sequencing to explore the molecular changes in iEGFR, DSS iEGFR lines,
426 and passage-matched controls. Principal component analysis established that replicate samples
427 clustered together with high reproducibility (Figure 2A). We found a total of 547 differentially expressed
428 genes in both types of iEGFR colonoids (absolute $\log_2$ fold change >2, Bonferroni-adjusted p-value <
429 0.05, Figure 2B, Supplementary Table 1, Supplementary Figure 4). Gene set enrichment analysis of the
430 upregulated overlapping genes (48) showed significant enrichment for genes associated with amine
431 transmembrane transporter activity, pyroptosis, and phosphatidylinositol-4-phosphate binding
432 pathways, while the overlapping downregulated genes (22) were involved in endocytosis and cell
433 junction assembly (Figure 2C). A subset of significantly differentially expressed genes was further
434 validated using quantitative reverse transcription polymerase chain reaction (qRT-PCR), including
435 those with roles in the EGF pathway, pyroptosis, and CRC carcinogenesis, such as *Igfpb7*, *Efemp1,*
436 *Gasdmc2, and Mycn* (Figure 2D; all tested genes validated). Taken together, these data show that key
437 neoplasia-relevant gene expression patterns emerge in colonic epithelial cells tolerant to EGF
438 withdrawal.

439 **iEGFR colonoids exhibit morphologic changes and increased proliferation**

440 Early epithelial neoplasia demonstrates characteristic morphological changes that have been routinely
441 used by pathologists to diagnose dysplasia and cancer for over a century[40]. Hematoxylin-and-eosin-
442 stained iEGFR colonoids show heterogeneous morphologic changes associated with dysplasia,
443 including nuclear hyperchromasia, pseudostratification, and increased nuclear-to-cytoplasmic ratio
444 (Figure 3A). DSS control colonoids showed features of reactive and regenerative epithelium, including
445 more squamoid cells with brightly eosinophilic cytoplasm. A subset of DSS iEGFR colonoids strikingly
446 showed loss of polarity and architectural complexity reminiscent of high-grade colitis-associated
447 dysplasia seen in patients with IBD (Figure 3A).

448 Neoplasia is also associated with sustained proliferation[41]. Our RNA-sequencing analysis revealed that
449 many genes associated with cellular proliferation were upregulated in iEGFR colonoids, including the
450 proto-oncogene *Mycn* (Figure 2D, Supplementary Table 1). To further explore this, we used a short-

451 pulse (6 hours) of the nucleotide analogue 5'-ethynyl-2'deoxyuridine (EdU) to analyze the proportion of
452 cells in the S-phase of the cell cycle in iEGFR colonoids. The proportion of EdU+ colonoids and percent
453 of EdU+ cells per colonoid were significantly higher in both iEGFR and DSS iEGFR colonoids
454 compared to their controls (Figure 3B-3D). These data show that the iEGFR phenotype is characterized
455 by histologic features of dysplasia and increased proliferation.

456 **iEGFR colonoids develop aneuploidy and chromosomal instability**

457 Loss of genomic integrity is one of the hallmarks of cancer, and chromosomal instability (CIN, or
458 ongoing aneuploidy) is observed in the majority of sporadic and IBD-associated CRC[2,41]. As aneuploidy
459 fuels adaptation to selective pressures[30,42], we hypothesized that this may play a role in acquisition of
460 iEGFR tolerance. As the long-term genetic stability of adult stem cell derived intestinal organoid
461 cultures has been established[43], as expected, metaphase spreads of control organoids were mostly
462 euploid (Figure 4A-B). In contrast, DSS-control colonoids were enriched for polyploidy (Figure 4A-B).
463 Previous literature has implicated *APC* loss in promoting CIN[44]; we observed both polyploidy and
464 aneuploidy in metaphase spreads of *Apc*^{mut} colonoids (Figure 4A).

465 We observed that heterogenous aneuploidy arose during iEGFR selection, with an overall tendency for
466 reduction in chromosomal number (subdiploid) (Figure 4A). Longer-term propagation of iEGFR
467 colonoids (more than 25 additional passages) resulted in convergence onto a gain of one chromosome
468 (Figure 4A, iEGFR 'H', or high passage)). Quantitative chromosome stoichiometry analysis via
469 quantitative PCR revealed a complete loss of chromosome 13 at an earlier passage (~12 passages
470 earlier than iEGFR 'H', Supplementary Figure 5). We hypothesized that aneuploidy could be due to
471 increased DNA damage, but did not detect increased double stranded breaks as assessed by γH2AX
472 staining in iEGFR colonoids relative to their corresponding controls (Supplemental Figure 6).

473 We next investigated the possibility that the heterogeneous aneuploidy was associated with ongoing
474 CIN. The dynamic properties of mitosis were quantified via live-imaging of 3D colonoid cultures of H2B-
475 mNeon expressing cells (Figure 4C-F, Supplementary Videos 1-6). The mean length of mitosis in
476 control colonoids was ~30 minutes, with errors detected in only 3-5% of all mitotic events (Figure 4C-D,
477 H). In contrast, iEGFR, *Apc*^{mut}, DSS control, and DSS iEGFR colonoids showed a significantly elevated
478 rate of erroneous mitoses relative to controls, ranging from approximately 20% (DSS lines) to 60%
479 (*Apc*^{mut}) (Figure 4D-E). In addition, the mean overall time of mitosis was significantly increased in DSS
480 control, DSS iEGFR, and *Apc*^{mut} organoids compared to control colonoids (Figure 4H), mostly driven by
481 increased length of nuclear envelope breakdown to chromosome alignment (Figure 4F-G).

482 Interestingly, altered mitotic timing was observed in DSS and *Apc*^{mut} lines but not in controls (Figure 4F-
483 H), suggesting defects in the spindle assembly checkpoint in these colonoids.

484 Finally, live imaging revealed a normal pattern of INM in most control colonoids undergoing mitosis
485 (Figure 5A), as previously described[14]. In contrast, this process was conspicuously absent in many
486 iEGFR, DSS control, DSS iEGFR, and *Apc*^{mut} mitoses (Figure 5A). Further, INM loss was significantly
487 associated with mitotic errors in our colonoid lines (Figure 5B-C).

488 Taken together, these data demonstrate that adaptation to long-term EGF withdrawal is associated with
489 mitotic defects that result in chromosomal instability and aneuploidy. In addition, we associate loss of
490 interkinetic nuclear migration with mitotic errors in colonic epithelium. Our data also show that prior
491 chronic mucosal injury predisposes to epithelial chromosomal instability that persists *ex vivo*.

492

493

494

495

496

497

498

499

500

501

502

503

504

505

506

507 **DISCUSSION**

508 Here, using long-term selective culture, we demonstrate that normal colonoids can adapt to withdrawal
509 of the critical niche factor EGF, a process associated with cytomorphologic features of dysplasia, loss
510 of INM, aneuploidy, CIN, somatic deleterious mutations, and transcriptional reprogramming. These data
511 support a scenario in which epithelial-autonomous molecular changes known to be associated with
512 neoplasia can arise during adaptation, the acquisition of which are accelerated by prior mucosal injury.
513
514 We discovered that iEGFR colonoids show aneuploidy and CIN (Figure 4) and are primed to adapt to
515 other niche-relevant selective pressures (Figure 1B). Genomic copy number changes were recently
516 shown to precede chronic inflammation-associated esophageal adenocarcinoma up to a decade prior
517 to histologic evidence of transformation[45], supporting an early initiating role for genomic instability.
518 Recent work has demonstrated low levels of spontaneous cell fusions (as we observed in iEGFR lines)
519 in cancer cell lines that led to increased phenotypic plasticity and accelerating adaptive potential[46].
520 Future work will determine whether CIN has a causal role in mediating iEGFR tolerance.
521
522 Carroll et al. demonstrated that INM is an important homeostatic mechanism involved in directing long-
523 term cell positioning in the intestinal crypt[14]. While approximately one third of normal mitoses with intact
524 INM led to separation of mitotic sisters, mitotic sisters always remained direct neighbors in the setting of
525 *Apc* mutation, potentially contributing to clonal expansion of early adenomas. Our data validate their
526 finding of INM loss with *Apc* mutation, which we further extend by associating INM loss with mitotic
527 errors in colonoid lines (Figure 5). While our live imaging data precluded definitive evaluation of post-
528 mitotic sister cell placement, it is possible that INM loss renders cells with mitotic errors more likely to
529 undergo clonal expansion.
530
531 Inflammation and mucosal injury reprograms colonic epithelium to a regenerative/progenitor-like
532 status[47–49], and in other organ systems, stem cell lineage infidelity drives both wound repair
533 (homeostatic) and cancer (pathogenic)[50,51]. Consistent with this literature, chronic DSS colonoids
534 showed enhanced adaptive potential to iEGFR selective culture (Figure 1A). In addition, we found
535 polyploidy in DSS colonoids, which has also been previously reported in the setting of wound repair
536 (Figure 4A-B)[52,53]. Our RNA-sequencing analysis revealed that genes related to pyroptosis were
537 significantly upregulated in iEGFR lines (Figure 2C-D). Pyroptosis, a caspase-dependent form of
538 proinflammatory programmed cell death, has emerging roles in the tumor microenvironment and has
539 been recently implicated in promoting colitis-associated cancer[54,55]. Recent investigation of somatic

evolution in IBD colonic epithelium revealed clonal expansions of mutations in the IL-17 pathway which render epithelium resistant to the IL-17A-induced pro-apoptotic response[56,57]. Whether aneuploidy similarly confers resistance to pyroptosis-associated cell death is a future avenue of exploration.

Prior studies indicate that human adenoma-derived colonoids are uniformly dependent on EGF in culture, similar to normal colonoids[3]. We were surprised to find that, in contrast to wild-type control colonoids, *Apc*^{mut} colonoids were not able to overcome withdrawal of EGF (Figure 1A). While it is well known that *KRAS/PIK3CA* wild-type CRC is susceptible to EGFR inhibition[58], our data suggest that this response may also be *APC* mutation-dependent.

Recent literature has demonstrated the presence of age-associated somatic mutations in normal non-dysplastic colonic epithelium across the lifespan with uncertain consequences[59–61]. Although rare patients with CRC harbor alterations in the somatically mutated genes we observed in iEGFR colonoids, whether these mutations act as drivers versus passengers in the adaptive iEGFR phenotype remains to be determined. We also acknowledge that bulk exome DNA sequencing may not detect rare mutations or mutations in regulatory elements that may contribute to the phenotype of our heterogeneous iEGFR colonoid lines.

Although further work is required to elucidate a potential role for perturbed niche homeostasis in human CRC initiation, our data support a potential role for microenvironmental selective pressures in promoting neoplastic transformation. Thus, increasing the granularity of our understanding of colon anatomic segment-specific mucosal microenvironments may reveal insights into the origins of distinct pathways of tumorigenesis (for example, the serrated versus adenomatous pathways of carcinogenesis in the proximal vs. distal colon, respectively).

In summary, we leveraged murine colonoids to demonstrate that sustained deprivation of niche-relevant growth factors alone can molecularly reprogram colonic epithelium. We anticipate that there are a spectrum of mechanisms epithelia can draw upon to adapt to such selective conditions. Tracking individual clones over time and extending our approaches to human and IBD-derived colonoid lines may determine whether adaptation mechanisms such as CIN are observed more broadly. Further, elucidating the mechanisms by which neoplasia-promoting epithelial phenotypes arise may reveal general vulnerabilities attractive for cancer prevention.

REFERENCES

1. Basak, O. *et al.* Induced Quiescence of Lgr5+ Stem Cells in Intestinal Organoids Enables Differentiation of Hormone-Producing Enteroendocrine Cells. *Cell Stem Cell* **20**, 177-190.e4 (2017).
2. Muzny, D. M. *et al.* Comprehensive molecular characterization of human colon and rectal cancer. *Nature* **487**, 330–337 (2012).
3. Fujii, M. *et al.* A Colorectal Tumor Organoid Library Demonstrates Progressive Loss of Niche Factor Requirements during Tumorigenesis. *Cell Stem Cell* **18**, 827–838 (2016).
4. Clevers, H. The intestinal crypt, a prototype stem cell compartment. *Cell* **154**, 274–84 (2013).
5. Powell, D. W., Pinchuk, I. V., Saada, J. I., Chen, X. & Mifflin, R. C. Mesenchymal Cells of the Intestinal Lamina Propria. *Annu. Rev. Physiol.* (2011) doi:10.1146/annurev.physiol.70.113006.100646.
6. Valenta, T. *et al.* Wnt Ligands Secreted by Subepithelial Mesenchymal Cells Are Essential for the Survival of Intestinal Stem Cells and Gut Homeostasis. *Cell Rep.* **15**, 911–918 (2016).
7. Sato, T. *et al.* Long-term Expansion of Epithelial Organoids From Human Colon, Adenoma, Adenocarcinoma, and Barrett's Epithelium. *Gastroenterology* **141**, 1762–1772 (2011).
8. van de Wetering, M. *et al.* Prospective Derivation of a Living Organoid Biobank of Colorectal Cancer Patients. *Cell* **161**, 933–945 (2015).
9. Kobayashi, H. *et al.* The balance of stromal BMP signaling mediated by GREM1 and ISLR drives colorectal carcinogenesis. *Gastroenterology* (2020) doi:10.1053/j.gastro.2020.11.011.
10. Drost, J. *et al.* Sequential cancer mutations in cultured human intestinal stem cells. *Nature* **521**, 43–47 (2015).
11. Matano, M. *et al.* Modeling colorectal cancer using CRISPR-Cas9–mediated engineering of human intestinal organoids. *Nat. Med.* **21**, 256–262 (2015).
12. Li, X. *et al.* Oncogenic transformation of diverse gastrointestinal tissues in primary organoid culture. *Nat. Med.* **20**, 769–777 (2014).
13. Ritsma, L. *et al.* Intestinal crypt homeostasis revealed at single-stem-cell level by in vivo live imaging. *Nature* **507**, 362–365 (2014).
14. Carroll, T. D. *et al.* Interkinetic nuclear migration and basal tethering facilitates post-mitotic daughter separation in intestinal organoids. *J. Cell Sci.* **130**, 3862–3877 (2017).
15. Kinchen, J. *et al.* Structural Remodeling of the Human Colonic Mesenchyme in Inflammatory Bowel Disease. *Cell* **175**, 372-386.e17 (2018).
16. Colotta, F., Allavena, P., Sica, A., Garlanda, C. & Mantovani, A. Cancer-related inflammation, the seventh hallmark of cancer: links to genetic instability. *Carcinogenesis* **30**, 1073–1081 (2009).
17. Coussens, L. M. & Werb, Z. Inflammation and cancer. *Nature* **420**, 860–867 (2002).
18. Holloway, E. M. *et al.* Mapping Development of the Human Intestinal Niche at Single-Cell Resolution. *Cell Stem Cell* (2020) doi:10.1016/j.stem.2020.11.008.
19. Fawkner-Corbett, D. *et al.* Spatiotemporal analysis of human intestinal development at single-cell resolution. *Cell* S009286742031686X (2021) doi:10.1016/j.cell.2020.12.016.
20. Ovid: Peptide growth factors in the intestine. http://ovidsp.dc2.ovid.com/ovid-b/ovidweb.cgi?T=JS&PAGE=fulltext&D=ovft&AN=00042737-200107000-00002&CHANNEL=CrossRef.
21. Eichele, D. D. & Kharbanda, K. K. Dextran sodium sulfate colitis murine model: An indispensable tool for advancing our understanding of inflammatory bowel diseases pathogenesis. *World J. Gastroenterol.* **23**, 6016–6029 (2017).
22. Chassaing, B., Aitken, J. D., Malleshappa, M. & Vijay-Kumar, M. Dextran sulfate sodium (DSS)-induced colitis in mice. *Curr. Protoc. Immunol.* **104**, 15.25.1-15.25.14 (2014).
23. Wirtz, S. *et al.* Chemically induced mouse models of acute and chronic intestinal inflammation. *Nat. Protoc.* **12**, 1295–1309 (2017).
24. Sato, T. *et al.* Paneth cells constitute the niche for Lgr5 stem cells in intestinal crypts. *Nature* **469**, 415–8 (2011).

625 25. Drost, J. *et al.* Sequential cancer mutations in cultured human intestinal stem cells. *Nature* **521**, 43–
626 47 (2015).
627 26. Schwank, G. & Clevers, H. CRISPR/Cas9-Mediated Genome Editing of Mouse Small Intestinal
628 Organoids. in *Gastrointestinal Physiology and Diseases: Methods and Protocols* (ed. Ivanov, A. I.)
629 3–11 (Springer, 2016). doi:10.1007/978-1-4939-3603-8_1.
630 27. Dekkers, J. F. *et al.* High-resolution 3D imaging of fixed and cleared organoids. *Nat. Protoc.* **14**,
631 1756–1771 (2019).
632 28. Bolhaqueiro, A. C. F. *et al.* Live imaging of cell division in 3D stem-cell organoid cultures. in (2018).
633 doi:10.1016/bs.mcb.2018.03.016.
634 29. Miura, K. *Temporal-Color Code (Version 101123)*
635 https://github.com/fiji/fiji/blob/master/plugins/Scripts/Image/Hyperstacks/Temporal-Color_Code.ijm
636 (2010).
637 30. Pavelka, N. *et al.* Aneuploidy confers quantitative proteome changes and phenotypic variation in
638 budding yeast. *Nature* **468**, 321–325 (2010).
639 31. Dobin, A. *et al.* STAR: ultrafast universal RNA-seq aligner. *Bioinforma. Oxf. Engl.* **29**, 15–21 (2013).
640 32. Liao, Y., Smyth, G. K. & Shi, W. The Subread aligner: fast, accurate and scalable read mapping by
641 seed-and-vote. *Nucleic Acids Res.* **41**, e108 (2013).
642 33. Love, M. I., Huber, W. & Anders, S. Moderated estimation of fold change and dispersion for RNA-
643 seq data with DESeq2. *Genome Biol.* **15**, 550 (2014).
644 34. Raudvere, U. *et al.* g:Profiler: a web server for functional enrichment analysis and conversions of
645 gene lists (2019 update). *Nucleic Acids Res.* **47**, W191–W198 (2019).
646 35. Kim, J. J., Shajib, M. S., Manocha, M. M. & Khan, W. I. Investigating intestinal inflammation in DSS-
647 induced model of IBD. *J. Vis. Exp. JoVE* (2012) doi:10.3791/3678.
648 36. Nowak, M. A. *et al.* The role of chromosomal instability in tumor initiation. *Proc. Natl. Acad. Sci. U.*
649 *S. A.* **99**, 16226–16231 (2002).
650 37. Moniz, S. *et al.* Protein kinase WNK2 inhibits cell proliferation by negatively modulating the
651 activation of MEK1/ERK1/2. *Oncogene* **26**, 6071–6081 (2007).
652 38. James, R. G. *et al.* Bruton's tyrosine kinase revealed as a negative regulator of Wnt-beta-catenin
653 signaling. *Sci. Signal.* **2**, ra25 (2009).
654 39. Yasuda, Y. *et al.* Human NINEIN polymorphism at codon 1111 is associated with the risk of
655 colorectal cancer. *Biomed. Rep.* **13**, 1–1 (2020).
656 40. Fischer, A. H. *et al.* The cytologic criteria of malignancy. *J. Cell. Biochem.* **110**, 795–811 (2010).
657 41. Hanahan, D. & Weinberg, R. A. *Hallmarks of cancer: The next generation*. *Cell* vol. 144 (2011).
658 42. Rancati, G. *et al.* Aneuploidy Underlies Rapid Adaptive Evolution of Yeast Cells Deprived of a
659 Conserved Cytokinesis Motor. *Cell* **135**, 879–893 (2008).
660 43. Huch, M. & Koo, B.-K. Modeling mouse and human development using organoid cultures.
661 *Development* **142**, 3113–3125 (2015).
662 44. Rusan, N. M. & Peifer, M. Original CIN: reviewing roles for APC in chromosome instability. *J. Cell*
663 *Biol.* **181**, 719–726 (2008).
664 45. Killcoyne, S. *et al.* Genomic copy number predicts esophageal cancer years before transformation.
665 *Nat. Med.* **26**, 1726–1732 (2020).
666 46. Miroshnychenko, D. *et al.* Spontaneous cell fusions as a mechanism of parasexual recombination
667 in tumour cell populations. *Nat. Ecol. Evol.* 1–13 (2021) doi:10.1038/s41559-020-01367-y.
668 47. Schwitalla, S. *et al.* Intestinal Tumorigenesis Initiated by Dedifferentiation and Acquisition of Stem-
669 Cell-like Properties. *Cell* **152**, 25–38 (2013).
670 48. Miyoshi, H. *et al.* Prostaglandin E2 promotes intestinal repair through an adaptive cellular response
671 of the epithelium. *EMBO J.* **36**, 5–24 (2017).
672 49. Yui, S. *et al.* YAP/TAZ-Dependent Reprogramming of Colonic Epithelium Links ECM Remodeling to
673 Tissue Regeneration. *Cell Stem Cell* **22**, 35-49.e7 (2018).
674 50. Dvorak, H. F. Tumors: Wounds That Do Not Heal—Redux. *Cancer Immunol. Res.* **3**, 1–11 (2015).

51. Ge, Y. *et al.* Stem Cell Lineage Infidelity Drives Wound Repair and Cancer. *Cell* **169**, 636-650.e14 (2017).
52. Losick, V. P. Wound-Induced Polyploidy Is Required for Tissue Repair. *Adv. Wound Care* **5**, 271–278 (2016).
53. Lucchetta, E. M. & Ohlstein, B. Amitosis of Polyploid Cells Regenerates Functional Stem Cells in the Drosophila Intestine. *Cell Stem Cell* **20**, 609-620.e6 (2017).
54. Tan, G., Huang, C., Chen, J. & Zhi, F. HMGB1 released from GSDME-mediated pyroptotic epithelial cells participates in the tumorigenesis of colitis-associated colorectal cancer through the ERK1/2 pathway. *J. Hematol. Oncol.J Hematol Oncol* **13**, 149 (2020).
55. Xia, X. *et al.* The role of pyroptosis in cancer: pro-cancer or pro-"host"? *Cell Death Dis.* **10**, 650 (2019).
56. Olafsson, S. *et al.* Somatic Evolution in Non-neoplastic IBD-Affected Colon. *Cell* S0092867420308138 (2020) doi:10.1016/j.cell.2020.06.036.
57. Nanki, K. *et al.* Somatic inflammatory gene mutations in human ulcerative colitis epithelium. *Nature* **577**, 254–259 (2020).
58. Khan, K. *et al.* Targeting EGFR pathway in metastatic colorectal cancer- tumour heterogeniety and convergent evolution. *Crit. Rev. Oncol. Hematol.* **143**, 153–163 (2019).
59. Lee-Six, H. *et al.* The landscape of somatic mutation in normal colorectal epithelial cells. *Nature* **574**, 532–537 (2019).
60. Nicholson, A. M. *et al.* Fixation and Spread of Somatic Mutations in Adult Human Colonic Epithelium. *Cell Stem Cell* **22**, 909-918.e8 (2018).
61. Smith, A. L. M. *et al.* Age-associated mitochondrial DNA mutations cause metabolic remodeling that contributes to accelerated intestinal tumorigenesis. *Nat. Cancer* **1**, 976–989 (2020).

714 **FIGURE LEGENDS**

715 **Figure 1. Colonoids adapt to culture conditions devoid of critical niche factors.**
716 **A)** Survival rate depicting viability of colonoids at the end of each selection cycle (7 days) as a
717 percentage of colonoid growth in control media (n= 6 biological replicates). **B)** Survival rate of colonoid
718 lines in other selective media after 7 days (n=3 biological replicates), **** $p < 0.0001$, 2-tailed non-
719 paired student t-test.
720

721 **Figure 2. Long-term adaptation of colonoids to EGF-deficient conditions results in**
722 **transcriptional changes.**
723 **A)** Samples analyzed by RNA-seq were plotted by principal component 1 (PC1) and principal
724 component 2 (PC2) using raw count data following regularized logarithm transformation. Samples from
725 the same experimental condition were grouped with the same colors. **B)** Volcano plots displaying $\log_2$-
726 transformed fold change and $-\log_{10}$-transformed *p* value of genes assessed by RNA-seq in iEGFR vs.
727 control colonoids and DSS iEGFR vs. DSS control colonoids. Selected differentially expressed genes
728 are highlighted. Genes highlighted in green are differentially expressed in both iEGFR and DSS iEGFR
729 compared to the respective control. Genes highlighted in red and blue are differentially expressed only
730 in iEGFR or DSS iEGFR, respectively. **C)** Gene set enrichment analysis of overlapping upregulated and
731 downregulated genes in both iEGFR and DSS iEGFR compared to the respective control. All enriched
732 gene sets (*p* value < 0.05) are shown. **D)** Quantitative RT-PCR validation of select upregulated (left)
733 and downregulated (right) genes detected by RNA-seq. Results are expressed as $\log_2$ fold change to
734 control and DSS control (n=3).
735

736 **Figure 3. iEGFR colonoids show morphologic features of dysplasia and increased proliferation.**
737 **A)** Representative H&E stained human tissues (upper panels, 20X) and cultured colonoids (lower
738 panels, 40X). Squares denote nuclear hyperchromasia and loss of nuclear polarity, arrowheads denote
739 architectural complexity, asterisks denote squamous features, and the triangle denotes overall normal
740 epithelial morphology. **B**) Representative confocal maximal Z-stacks images for colonoids stained with
741 the thymidine analogue EdU (green) and the counterstain DAPI (blue). No-EdU and Nutlin served as
742 negative and positive controls, respectively. Scale bars = 50 μm. n = 3 independent experiments. C)
743 Box and whiskers plot for the percentage of EdU positive nuclei per EdU-positive colonoid. Transverse
744 lines represent the median, boxes show 25th-75th percentile and the whiskers represent the lowest and
745 highest values within 1.5 times the interquartile range. **** $p < 0.0001$, *$p \leq 0.05$; 2-tailed, non-paired
746 student t-test. **D)** Bar plot for the percentage of colonoids with at least one EdU positive cell (n= 3

747 biological replicates). Error bars represent standard deviation. ****$p < 0.0001$, *$p \leq 0.05$; 2-tailed, non-
748 paired student t-test.
749
750 **Figure 4. iEGFR colonoids are aneuploid and demonstrate chromosomal instability.**
751 **A)** Dot plot of the number of chromosomes in metaphase spreads. The number of counted spreads and
752 the percentage of metaphase spreads with euploid chromosomes are shown at the top. The red line
753 represents tetraploidy. iEGFR(H) and iEGFR(L) correspond to high passage number ('H' high, passage
754 66) and lower passage number ('L' low, passage 40), respectively. **B)** Representative images of
755 metaphase spreads from control (euploid) and DSS control (tetraploid) colonoids. 60x. **C)**
756 Representative color depth coded images of chromosome segregation errors as revealed by H2B-
757 mNeon labeling of colonoids. Insets highlight mitoses in white boxes. White arrows indicate mitotic
758 errors, corresponding to Supplementary Videos 1-6. n= 4 or 5 independent experiments. **D)** Box and
759 whiskers plot of the percentage of segregation errors. Transverse lines represent the median, boxes
760 show 25th-75th percentile and the whiskers represent the lowest and highest values within 1.5 times the
761 interquartile range. The number of divisions and colonoids analyzed are shown at the top.
762 ****$p < 0.0001$, *$p \leq 0.05$; 2-tailed, non-paired student t-test. **E)** Bar plot of the percentage of different
763 segregation errors in analyzed mitotic figures. Other types of errors include multipolar mitoses, mitotic
764 failure, and fusion of nuclei. **F-H)** Illustrative cartoons and violin plots for time distribution of duration
765 from nuclear envelope breakdown (NEB) to chromosome alignment (F), chromosome alignment to
766 completion of mitosis (G), and total mitotic time (H). Transverse solid lines represent the median and
767 the dotted lines border 25th -75th percentiles. ****$p < 0.0001$, *$p \leq 0.05$; 2-tailed, non-paired student t-
768 test.
769
770 **Figure 5. INM loss is frequent in iEGFR colonoids and significantly associated with mitotic**
771 **errors.**
772 **A)** Sequential still images captured from representative individual mitoses (highlighted by white
773 arrowheads) as revealed by H2B-mNeon labeling of control, iEGFR, and *Apc*^{mut} colonoids. **B)** Bar
774 graph stratifying the presence of mitotic errors with the presence (n=79) or loss (n=98) of INM in all
775 analyzed mitoses across colonoid lines. ****$p < 0.0001$; 2-tailed Fisher's exact test. **C)** Bar graph
776 detailing the percentage of mitoses with INM loss in each colonoid line. The number of mitoses and
777 colonoids evaluated per group are shown at top. ***$p < 0.001$, *$p \leq 0.05$; 2-tailed Fisher's exact test.
778
779 **Table 1. iEGFR colonoids acquire rare high-impact protein-coding mutations.**

780 **SUPPLEMENTARY FIGURES, TABLES, AND VIDEOS**

781

782 **Supplementary Figure 1. A)** Representative confocal fluorescence images (Z sections with maximum
783 projection) of cleared colonoids labeled with chromogranin A (CHGA, green) and the counter stain
784 DAPI (blue). **B)** Bar plot illustrating the number of chromogranin A positive cells per colonoid, evidence
785 of enteroendocrine differentiation. Error bars represent standard deviation. *** p <0.001. **C)** Bar plot
786 demonstrating the survival rate of iEGFR colonoids after re-challenging with iEGFR and other selective
787 media after 3 weeks in EGF-replete media, relative to control.

788

789 **Supplementary Figure 2. A)** Bar plot for the ratio of body weight to colon length in mice treated with
790 DSS in water vs. water only control. Error bars represents standard deviation. n=3. **B)** Representative
791 H&E sections of colons from a DSS-treated (right) and a control mouse (left).

792

793 **Supplementary Figure 3. A)** Targeting sites and sgRNA that were used to target *Apc* in normal mouse
794 colonoids. **B)** Whole exome sequencing of Apc^{mut} colonoids confirms the presence of biallelic truncating
795 mutations at the expected site of targeted CRISPR/Cas9 genome editing. **C)** Representative brightfield
796 images of Apc^{mut} colonoids with characteristic spheroid morphology, as well as representative image
797 from other colonoid lines. **D)** Representative brightfield images of colonoid lines corresponding to Day 0
798 and Day 7 of the selective challenges detailed in Figure 1B.

799

800 **Supplementary Figure 4.** The number of differentially expressed genes in iEGFR colonoids relative to
801 control organoids, $\log_2$ fold changes ≥ 2 and Bonferroni p-value < 0.05. **A)** upregulated genes, **B)**
802 downregulated genes.

803

804 **Supplementary Figure 5.** Chromosome copy number in control (euploid) and higher-passage iEGFR
805 colonoids (~passage 54, aneuploid) quantified by qPCR, indicating loss of one copy of chromosome
806 13. n = 3 technical replicates.

807

808 **Supplementary Figure 6. A)** Representative confocal fluorescence images (Z sections with maximum
809 projection) of colonoids stained with γH2AX antibodies (red) and DAPI (blue). Doxorubicin and No Ab
810 (no antibody) represent the positive and negative controls, respectively. Scale bars = 50μm. **B)** The
811 percentage of γH2AX positive cells/colonoid is represented as a box and whisker plot. Transverse lines
812 represent the median, boxes show 25th-75th percentile and the whiskers represent the lowest and

813 highest values within 1.5 times the interquartile range. ns = not statistically significant, $p \geq 0.05$ 2-tailed,
814 non-paired student t-test.
815
816
817 **Supplementary Table 1.** Unfiltered differentially expressed genes in iEGFR and DSS iEGFR colonoid
818 lines vs. their respective controls.

819 **Supplementary Table 2.** Mouse primer sequences for chromosome karyotyping by qRT-PCR.

820 **Supplementary Table 3.** Mouse primer sequences for qRT-PCR validation of RNA-seq data

821

822 **Supplementary Video 1 (Control colonoids)**

823 Example of normal cell division.

824 **Supplementary Video 2 (iEGFR colonoids)**

825 Example of an erroneous division with a multipolar mitosis.

826 **Supplementary Video 3 (iEGFR colonoids)**

827 Example of an erroneous division with an anaphase bridge.

828 **Supplementary Video 4 (DSS control colonoids)**

829 Example of an erroneous division with a lagging chromosome.

830 **Supplementary Video 5 (DSS iEGFR colonoids)**

831 Example of an erroneous division with mitotic failure.

832 **Supplementary Video 6 (*Apc*^{mut} colonoids)**

833 Example of lagging chromosomes.

834

835

836

Figure 1

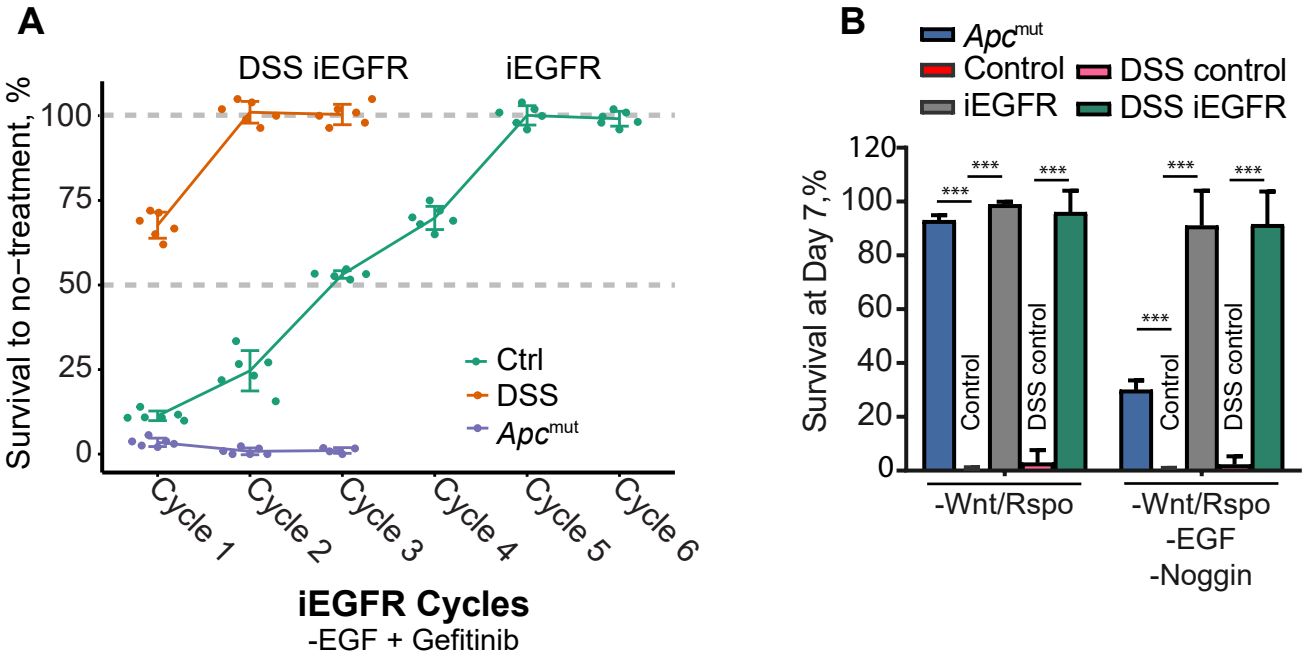
A
DSS iEGFR
iEGFR
Survival to no−treatment, %
100
75
50
25
0
Ctrl
DSS
Apcmut
Cycle 1
Cycle 2
Cycle 3
Cycle 4
Cycle 5
Cycle 6
iEGFR Cycles
-EGF + Gefitinib
B
Apcmut
Control
DSS control
iEGFR
DSS iEGFR
Survival at Day 7,%
120
100
80
60
40
20
0
***
Control
DSS control
-Wnt/Rspo
-Wnt/Rspo
-EGF
-Noggin

Figure 2

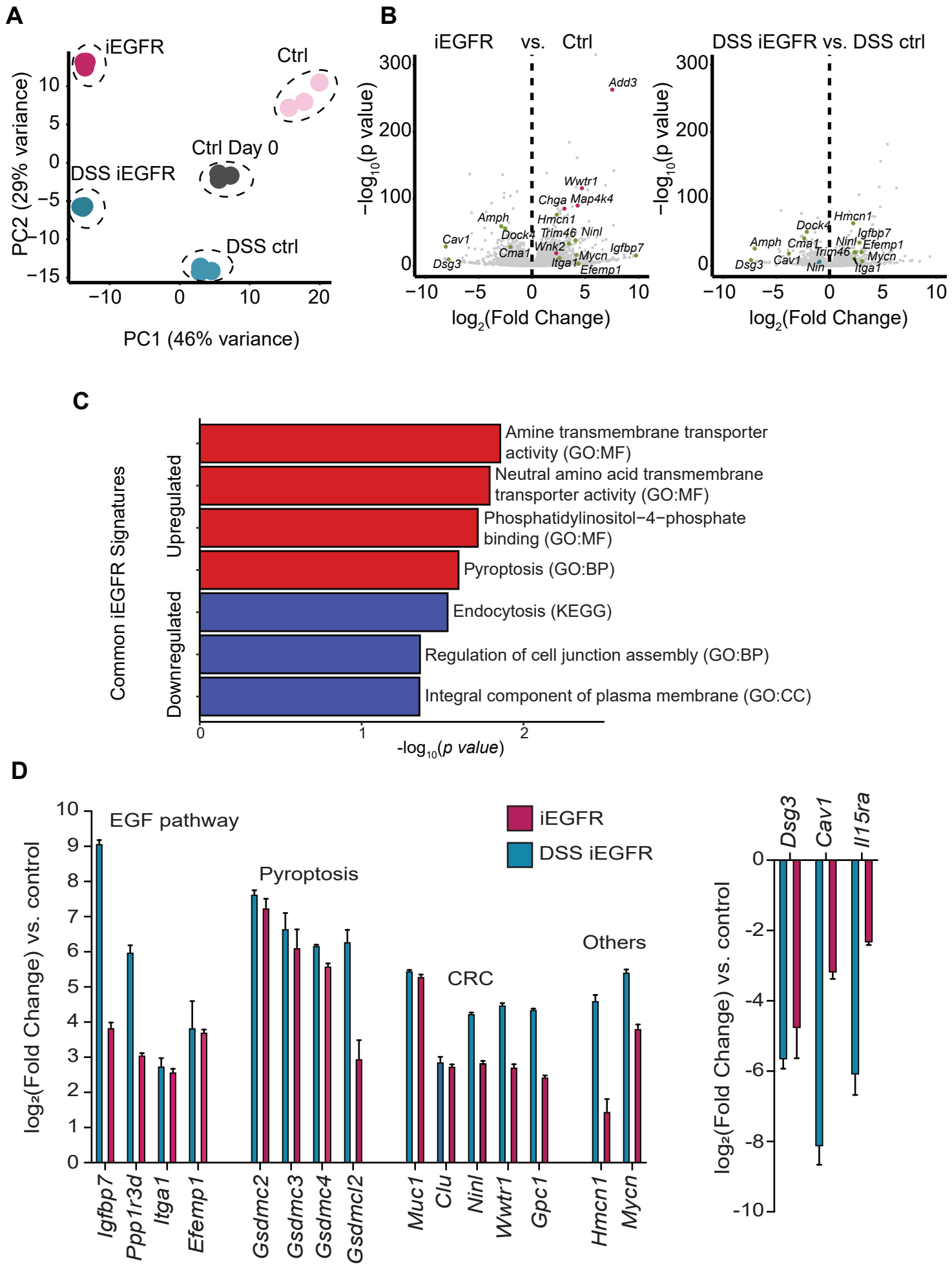
A
iEGFR
Ctrl
Ctrl Day 0
DSS iEGFR
DSS ctrl
PC2 (29% variance)
PC1 (46% variance)
B
iEGFR vs. Ctrl
DSS iEGFR vs. DSS ctrl
−log10(p value)
log2(Fold Change)
Add3
Wwtr1
Chga
Map4k4
Amph
Hmcn1
Dock4
Trim46
Ninl
Cav1
Cma1
Wnk2
Igfbp7
Mycn
Dsg3
Itga1
Efemp1
C
Common iEGFR Signatures
Upregulated
Downregulated
Amine transmembrane transporter activity (GO:MF)
Neutral amino acid transmembrane transporter activity (GO:MF)
Phosphatidylinositol−4−phosphate binding (GO:MF)
Pyroptosis (GO:BP)
Endocytosis (KEGG)
Regulation of cell junction assembly (GO:BP)
Integral component of plasma membrane (GO:CC)
-log10(p value)
D
EGF pathway
Pyroptosis
CRC
Others
iEGFR
DSS iEGFR
log2(Fold Change) vs. control
Igfbp7
Ppp1r3d
Itga1
Efemp1
Gsdmc2
Gsdmc3
Gsdmc4
Gsdmcl2
Muc1
Clu
Ninl
Wwtr1
Gpc1
Hmcn1
Mycn
Dsg3
Cav1
Il15ra

Figure 3

A

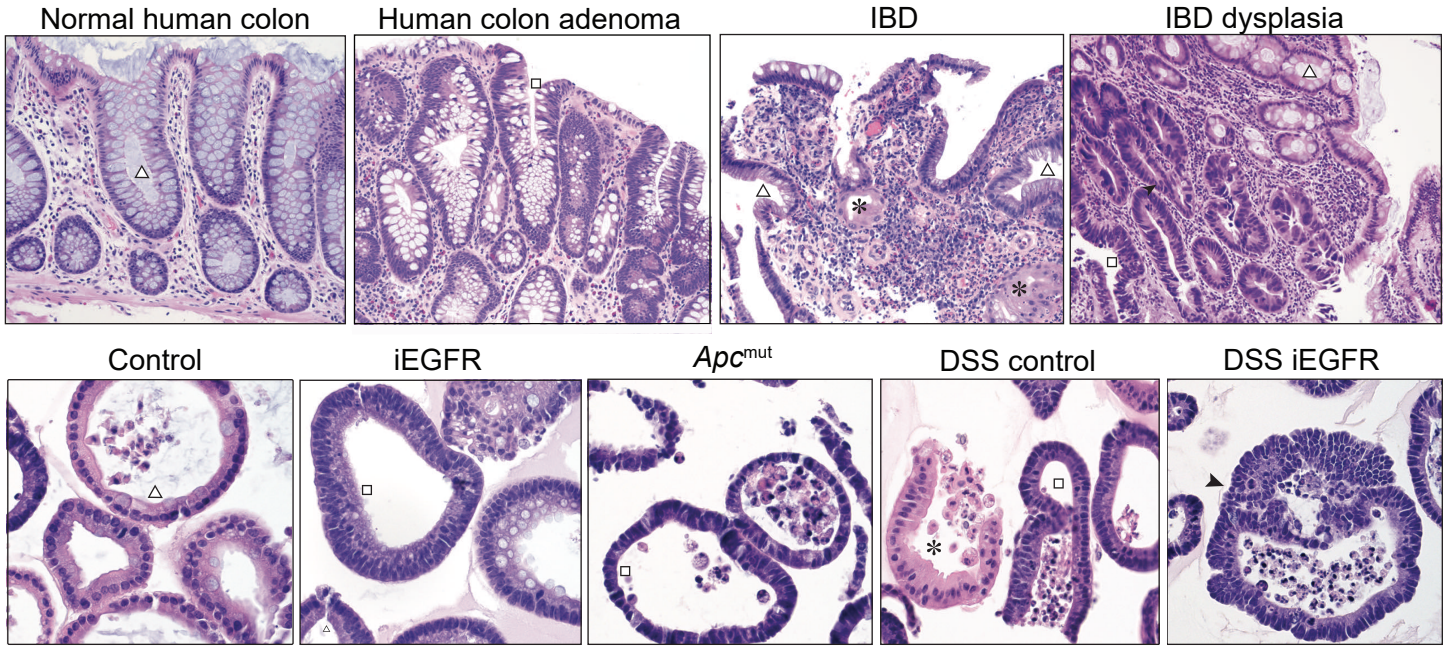

B

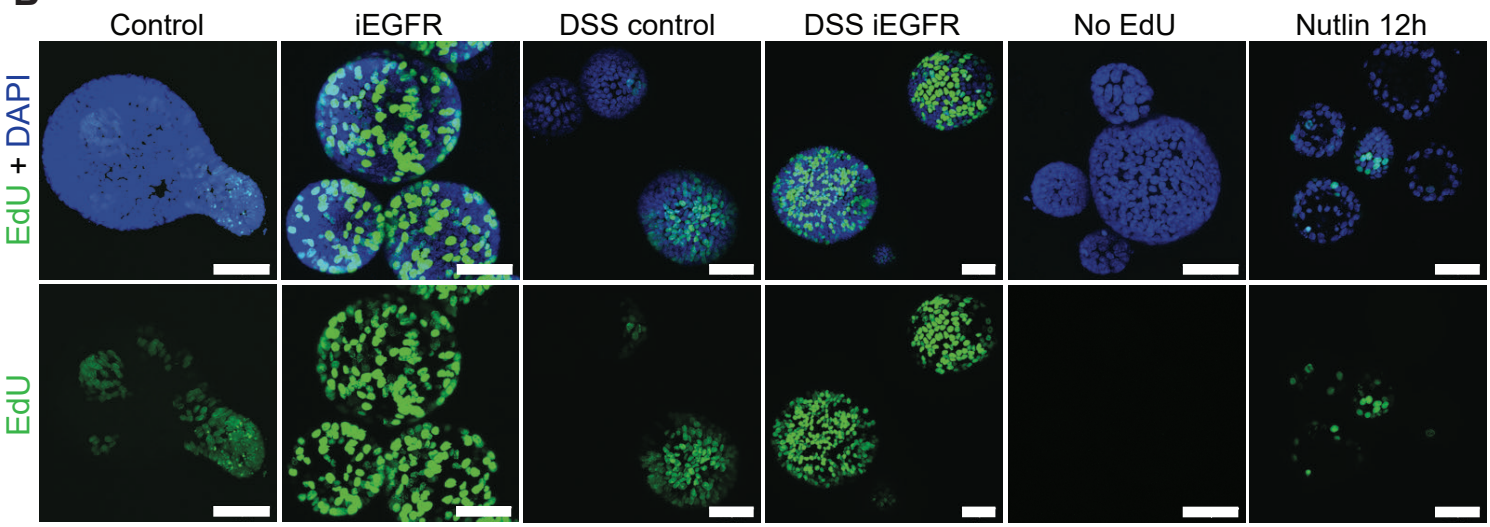

C

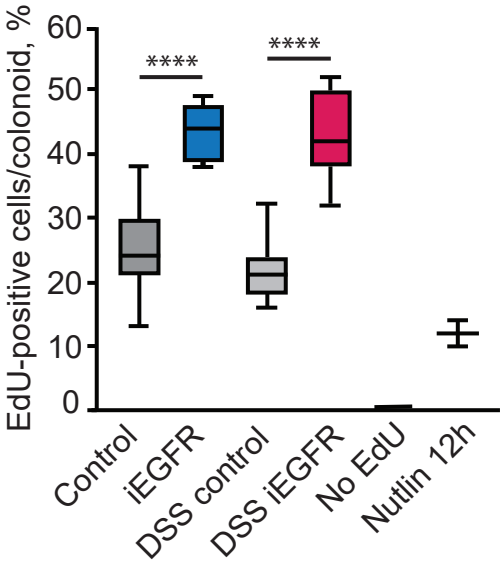

D

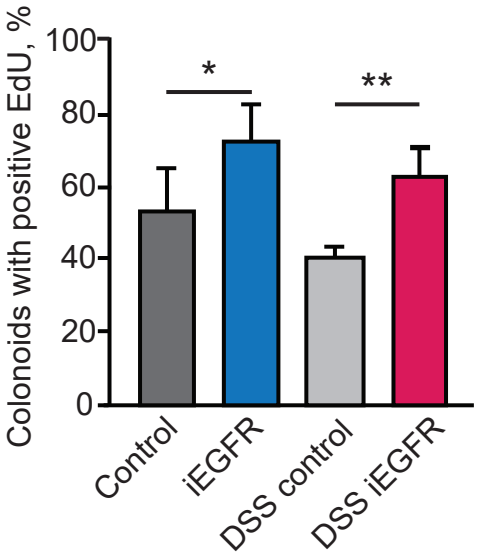

Figure 4

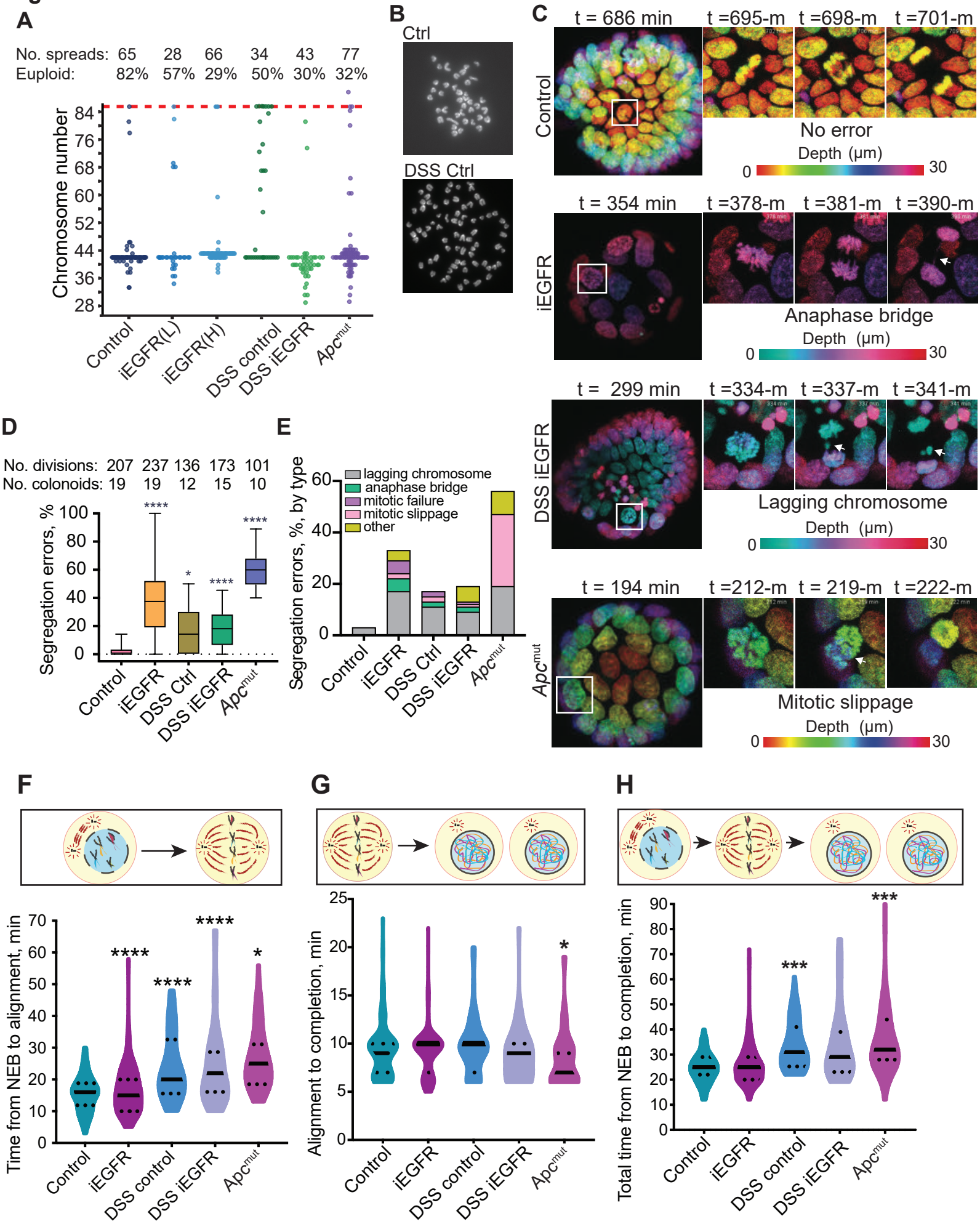
A
No. spreads: 65 28 66 34 43 77
Euploid: 82% 57% 29% 50% 30% 32%
Chromosome number
84
76
68
60
52
44
36
28
Control
iEGFR(L)
iEGFR(H)
DSS control
DSS iEGFR
Apcmut
B
Ctrl
DSS Ctrl
C
t = 686 min
t =695-m
t =698-m
t =701-m
Control
No error
Depth (μm)
0
30
t = 354 min
t =378-m
t =381-m
t =390-m
iEGFR
Anaphase bridge
Depth (μm)
0
30
t = 299 min
t =334-m
t =337-m
t =341-m
DSS iEGFR
Lagging chromosome
Depth (μm)
0
30
t = 194 min
t =212-m
t = 219-m
t =222-m
Apcmut
Mitotic slippage
Depth (μm)
0
30
D
No. divisions: 207 237 136 173 101
No. colonoids: 19 19 12 15 10
Segregation errors, %
100
80
60
40
20
0
****
*
****
****
Control
iEGFR
DSS Ctrl
DSS iEGFR
Apcmut
E
Segregation errors, %, by type
60
40
20
0
lagging chromosome
anaphase bridge
mitotic failure
mitotic slippage
other
Control
iEGFR
DSS Ctrl
DSS iEGFR
Apcmut
F
Time from NEB to alignment, min
70
60
50
40
30
20
10
0
****
****
****
*
Control
iEGFR
DSS control
DSS iEGFR
Apcmut
G
Alignment to completion, min
25
20
15
10
5
0
*
Control
iEGFR
DSS control
DSS iEGFR
Apcmut
H
Total time from NEB to completion, min
90
80
70
60
50
40
30
20
10
0
***
***
Control
iEGFR
DSS control
DSS iEGFR
Apcmut

Figure 5

A

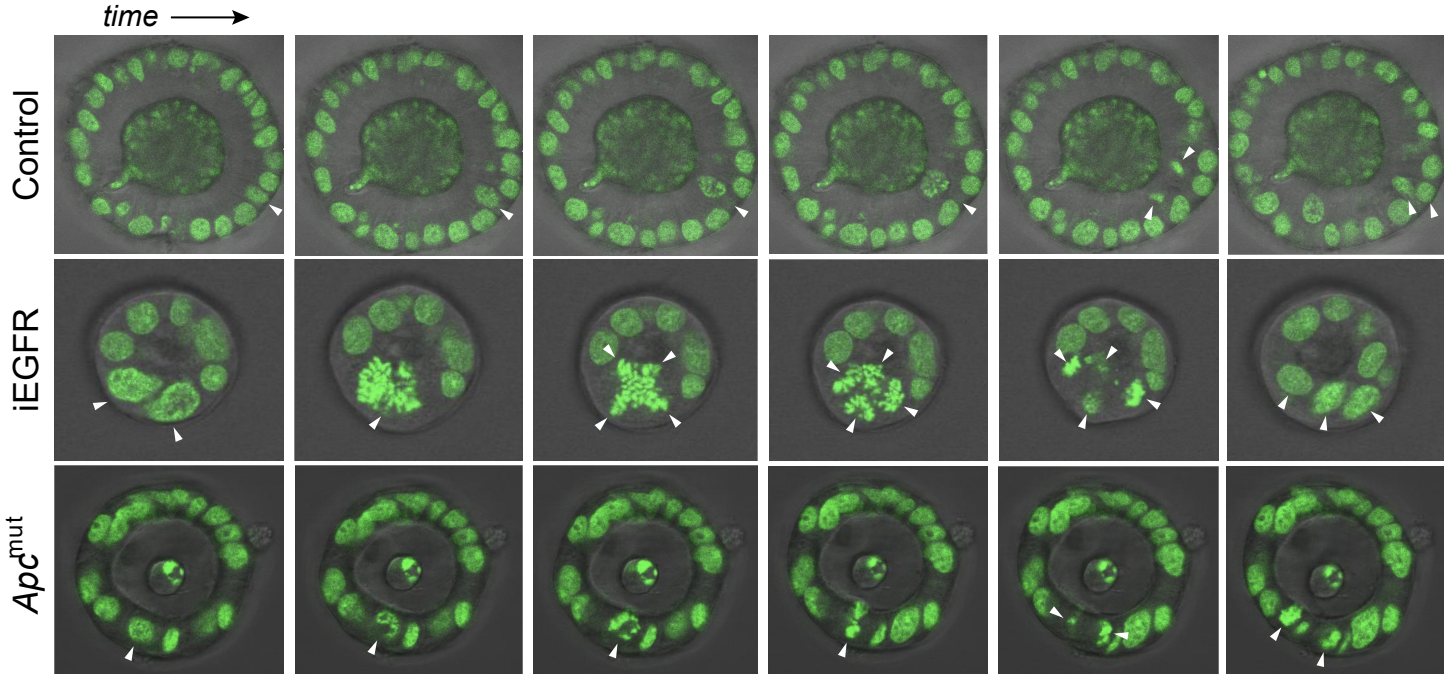
time
Control
iEGFR
Apc^mut

B

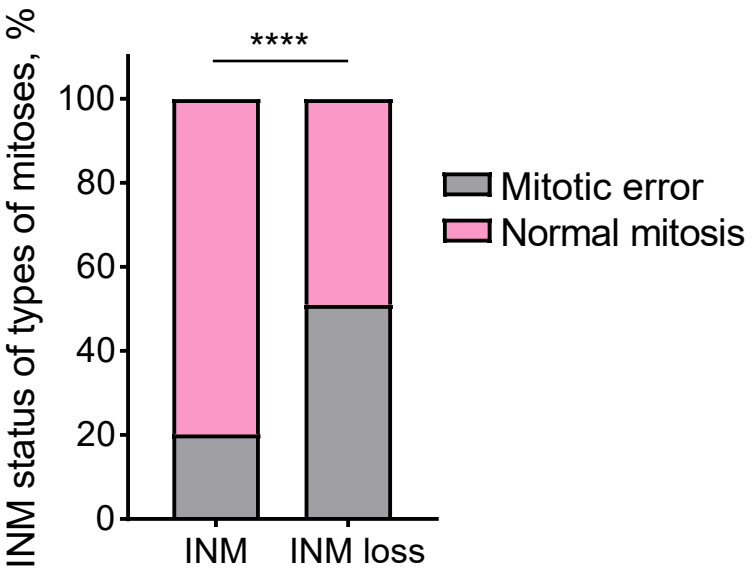
INM status of types of mitoses, %
****
100
80
60
40
20
0
INM
INM loss
Mitotic error
Normal mitosis

C

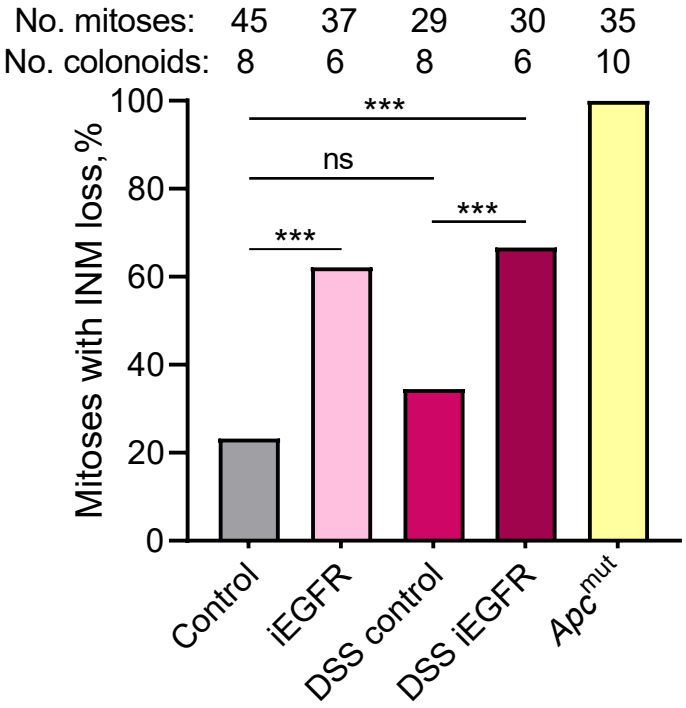
No. mitoses: 45 37 29 30 35
No. colonoids: 8 6 8 6 10
Mitoses with INM loss,%
100
80
60
40
20
0
***
ns
***
***
Control
iEGFR
DSS control
DSS iEGFR
Apc^mut

Table 1. Summary of mutations identified in iEGFR colonoids by WES.

Sample	Chr	Gene	Mutation	VAF (reads)	Mutation Type	Known function of gene product	Frequency of gene alteration in human CRC patients
iEGFR	X	*Btk*	p.Lys573*/c.1717A>T	48% (48/52)	Nonsense	Negative regulator of Wnt-β-catenin signaling	26/3407 (0.8%)
iEGFR	2	*Olfr1255*	p.Ile210fs/c.628_629delAT	38% (57/151)	Frameshift	Olfactory receptor	N/A
iEGFR	17	*Treml2*	p.Trp76*/c.227G>A	48% (45/93)	Nonsense	Roles in innate and adaptive immunity	1/3407 (0.03%)
iEGFR	13	*Wnk2*	p.Thr751fs/c.2249insC	60% (6/10)	Frameshift	Negative regulator of EGF-induced activation of the ERK/MAPK-pathway, cell cycle progression	5/3407 (0.1%)
DSS iEGFR	12	*Ninein*	p.Gln114*/c.340C>T	27% (31/113)	Nonsense	Centrosomal protein, microtubule anchoring	23/3407 (0.7%)

Predicted high-impact mutations detected by WES performed on iEGFR lines and respective controls. With the exception of *Ninein,* these mutations were not detected in control lines (passage matched for control). *Ninein* mutation was found at 13% VAF (12/85 reads) in the DSS control line, and at 27% VAF in DSS iEGFR (31/113 reads). Genetic alterations were queried from publicly available data in cBioPortal, and excluded germline variants and variants of unknown significance.